

Supporting Information for:

Observation of an Internal *p-n* Junction in Pyrite FeS₂ Single Crystals: Potential Origin of the Low Open Circuit Voltage in Pyrite Solar Cells

Bryan Voigt¹, William Moore¹, Moumita Maiti¹, Jeff Walter^{1,2}, Bhaskar Das¹, Michael Manno¹,
Chris Leighton*¹, and Eray S. Aydil*^{1,3}

¹*Department of Chemical Engineering and Materials Science,
University of Minnesota, Minneapolis, MN 55455, USA*

²*Department of Physics,
Augsburg University, Minneapolis, MN 55454, USA*

³*Department of Chemical and Biomolecular Engineering,
New York University Tandon School of Engineering, Brooklyn, NY 11201, USA*

*Corresponding authors: aydil@nyu.edu, leighton@umn.edu

A. Band bending calculations

Band energies and carrier densities as a function of depth from the pyrite crystal surface were calculated using 1D Poisson, a software package by G. Snider.¹ As concluded elsewhere,² the sulfur vacancy (V_S)-doped pyrite crystal interior can be described as a compensated *n*-type semiconductor, with a band gap (E_g) of 0.95 eV, and thus electron density (n) given by

$$n(T) = \frac{N_C(N_D - N_A)}{N_A} e^{-\Delta E/k_B T}, \quad (\text{S1})$$

where T is temperature, ΔE is the thermal activation energy ($\Delta E = 0.225$ eV in the light doping limit for V_S), N_C is the effective density-of-states in the conduction band ($\sim 7.6 \times 10^{18}$ cm⁻³ for pyrite), N_D is the donor density, N_A is the (compensating) acceptor density, and k_B is Boltzmann's constant.^{2,3} For the specific example calculations in Figure 1a of the main text, $N_D = 9.3 \times 10^{18}$ cm⁻³ and $N_A = 7.5 \times 10^{17}$ cm⁻³; Voigt *et al.*² outline how these quantities were previously determined. The crystal surface was modeled as *p*-type, with sufficient band bending to pin the Fermi level (E_F) at 100 meV above the valence band maximum to agree with ultraviolet photoelectron spectroscopy (UPS), X-ray photoelectron spectroscopy (XPS), and transport measurements.⁴⁻⁸ Subsequently calculated band energies and carrier densities are shown in Figure 1a of the main text. In this lightly-V_S-doped case, ~ 650 meV of band bending occurs. In heavily-V_S-doped crystals (*e.g.*, those grown at low S vapor pressures), ΔE falls to ~ 25 meV and band bending of 750-825 meV (dependent on T and the compensation ratio) is expected, as noted in the text.

B. Time-of-flight secondary ion mass spectrometry depth profiles

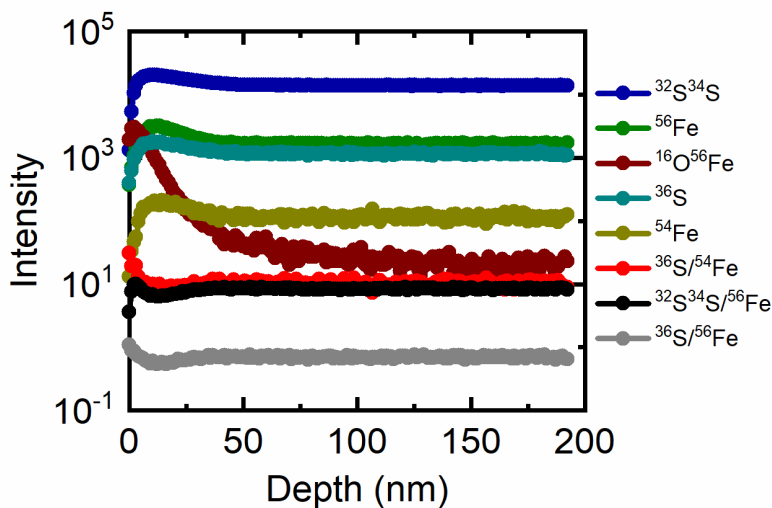


Figure S1. Negative-ion time-of-flight secondary ion mass spectrometry (TOF-SIMS) depth-profiles of a polished crystal. SIMS was acquired with 30 keV Bi^+ and a raster size of $100 \times 100 \mu\text{m}$; 1 kV Cs^+ and a $500 \times 500 \mu\text{m}$ raster size was used for sputtering. Intensity ratios are also shown, giving qualitative S:Fe stoichiometry as a function of depth. Other than a small ($\sim 20\%$) shift within ~ 30 nm of the crystal surface, the ratios of S to Fe intensities (red, black, and grey points) show no depth-dependence in the top ~ 200 nm of crystals. A small near-surface decrease in S/Fe can be easily accounted for by surface oxidation, which is well-known to change secondary ion yields; in particular, it drives higher yields from less electronegative atoms (Fe here), causing an artificial decrease in S/Fe intensity ratios. Indeed, the strong near-surface $^{16}\text{O}^{56}\text{Fe}$ intensity falls off very close to this depth, confirming that oxygen causes this small shift. Our crystals thus have rather uniform stoichiometry from the surface to the bulk.

C. Sheet resistance data in Figure 2 of the main text converted to resistivity

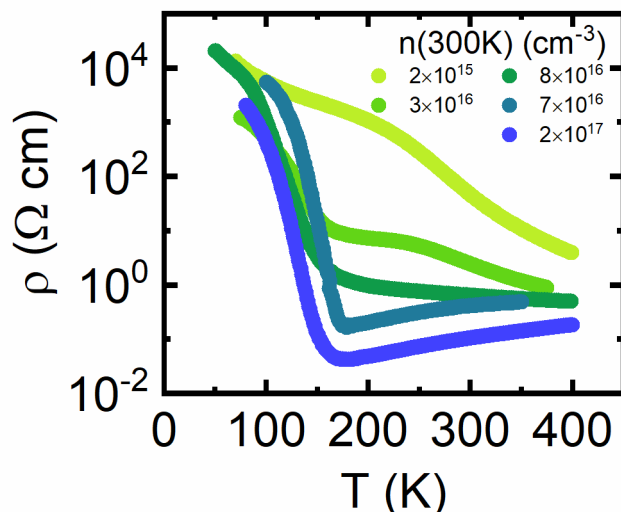


Figure S2. Temperature (T) dependence of the *resistivity* (ρ) of V_S -doped pyrite crystals. V_S doping is systematically increased by decreasing S vapor pressure during crystal growth, increasing room temperature electron densities ($n(300K)$) from $2 \times 10^{15} \text{ cm}^{-3}$ (light green data) to $2 \times 10^{17} \text{ cm}^{-3}$ (blue data), driving a corresponding strong decrease in ρ (e.g., nearly three orders of magnitude at 300 K). Compare to Figure 2 of the main text. Adapted with permission from (Voigt, B.; Moore, W.; Manno, M.; Walter, J.; Jeremiason, J.D.; Aydil, E.S.; Leighton, C. Transport Evidence for Sulfur Vacancies as the Origin of Unintentional n -Type Doping in Pyrite FeS_2 . *ACS Appl. Mater. Interfaces* **2019**, 11, 15552-15563).² Copyright (2019) American Chemical Society.

D. V_S -doping independence of surface conduction: Comparing surface conduction in crystals grown at high and low S vapor pressures

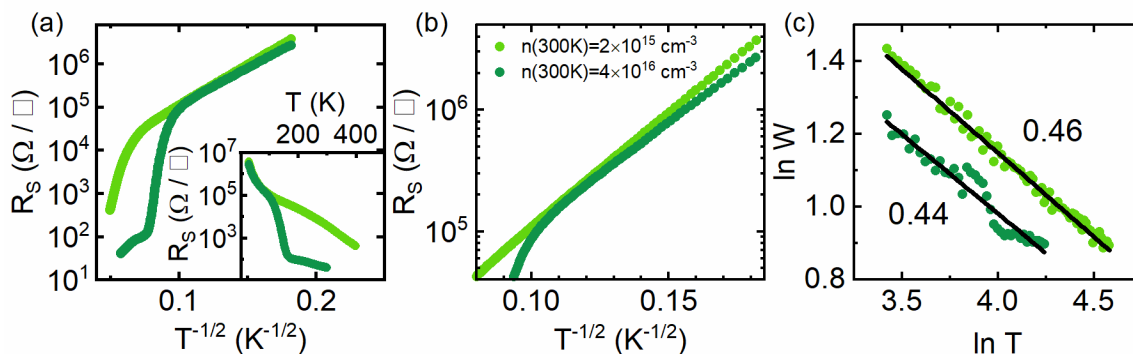


Figure S3. (a,b) Sheet resistance (R_S) vs. $T^{-1/2}$ for pyrite crystals grown at high (light green) and low (dark green) S pressures. Room temperature electron densities ($n(300K)$) denote the level of V_S doping, with lower vapor pressures yielding higher $n(300K)$. The inset in (a) shows R_S vs. T for the same data, and (b) is a magnification of the low T region in (a). (c) Zabrodskii plot ($\ln W$ vs. $\ln T$, where $W = -d(\ln R)/d(\ln T)$) showing data (points) from 30-100 K, linear fits (black lines), and corresponding m values (slope = $-m$). The transport mechanism at low T deduced from these slopes is Efros-Shklovskii variable range hopping (ES-VRH), i.e., $m \approx 1/2$ in $R_S = R_0 e^{(T_0/T)^m}$.^{9,10}

E. $R_S(T)$ in heavily- V_S -doped crystals contacted using different metals and using different approaches

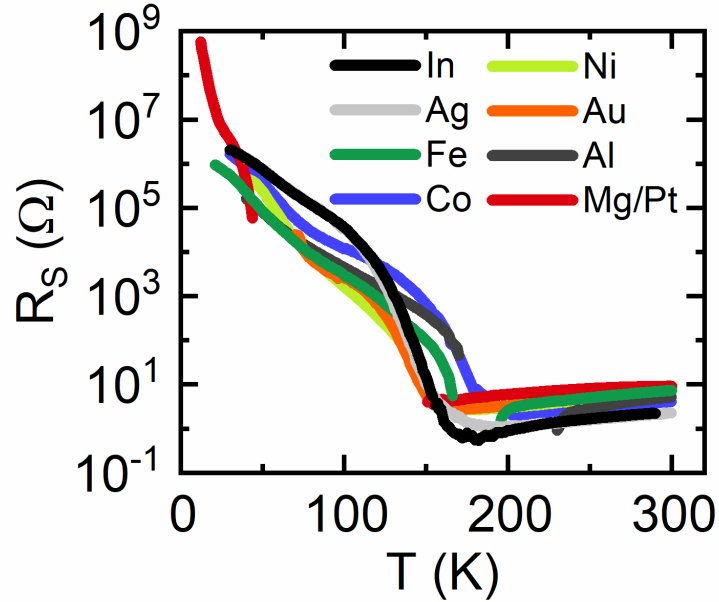


Figure S4. Temperature (T)-dependence of the sheet resistance (R_S) of heavily- V_S -doped crystals contacted with various metals and in different ways (sputtering, soldering, *etc.*). Specifically, contacts were made using Ag paste, soldering (In), sputtering (Mg/Pt, Ni, Fe, Au), and evaporation (Co, Al). Note the strong similarity, regardless of contact metal and method.

F. Modeling of the n -type interior resistance (R_I)

In the main text, the resistance of the n -type interior, R_I , is described using diffusive transport, *i.e.*, $R_I = (qn\mu t)^{-1}$, where q is the electronic charge, and $n(T)$ and $\mu(T)$ are the temperature-dependent electron density and mobility, respectively. Most simply, $n(T)$ can be described by replacing $\frac{N_C(N_D - N_A)}{N_A}$ in equation S1 above with a single quantity, n_∞ , representing the $T \rightarrow \infty$ extrapolation of $n(T)$. The parameters ΔE and n_∞ can then be determined from an Arrhenius fit to $n(T)$. For example, such a fit is shown in Figure S5a below for the crystal grown at high S vapor pressure ($n(300\text{K}) = 2 \times 10^{15} \text{ cm}^{-3}$: Figure 3a of the main text), yielding $\Delta E = 252 \text{ meV}$ and $n_\infty = 3.2 \times 10^{19} \text{ cm}^{-3}$. This ΔE is consistent with the native V_S donor level recently identified.² In the crystal grown at a moderate S pressure (Figure 3e of the main text), $n(300 \text{ K})$ is $\sim 8 \times 10^{16} \text{ cm}^{-3}$, demonstrating increased V_S doping. The data in Figure 3e and the corresponding Arrhenius analysis (Figure S5b) show a clear decrease in activation energy, indicating that these V_S concentrations are high enough to initiate donor band broadening and an evolution towards an insulator-metal transition. Furthermore, *two* apparent activation energies, each describing $n(T)$ in a different T range, are now evident in Figure S5b. These are denoted ΔE_1 and ΔE_2 , where $\Delta E_1 = 78 \text{ meV}$ describes n at higher T (235-400 K) and $\Delta E_2 = 19 \text{ meV}$ describes n at lower T (150-235 K). At even lower S pressure, V_S doping is further increased, yielding $n(300 \text{ K}) = 2 \times 10^{17} \text{ cm}^{-3}$

(Figure 3i). Two activation energies are again observed on the corresponding Arrhenius plot (Figure S5c), with $\Delta E_1 = 24$ meV and $\Delta E_2 = 4$ meV, demonstrating yet closer approach to the insulator-metal transition. Note that the fits yielding ΔE_2 are performed over limited ranges here, as the junction shuts off access to R_1 below ~ 150 K, restricting our observation of ΔE_2 to a modest T range. Clearly, mitigating the internal p - n junction would allow wider- T -range access to ΔE_2 . Note also that two ΔE s are only observed when the V_S -doping generates $n(300\text{ K}) \gtrsim 3 \times 10^{16} \text{ cm}^{-3}$. We do not yet understand the precise origin of the two ΔE s because the specific V_S -containing defects (or complexes) responsible for n -doping are not known with high confidence in pyrite. Density functional theory calculations indicate that V_S clusters play an important role in doping pyrite FeS_2 n -type and these could potentially yield two ΔE s from distinct levels in the gap.¹¹ The mobilities are also too large for hopping transport, ruling out that the lower ΔE could result from nearest neighbor hopping. Regardless, and most important in the current context, $n(T)$ is readily described by simple activation, with the $n_{\infty,i}$ and ΔE_i values shown in Table 1 of the main text for each crystal in this study. When two regimes of activation are evident, $n_{\infty,1}$ and ΔE_1 describe $n(T)$ at high T , and $n_{\infty,2}$ and ΔE_2 describe $n(T)$ at low T ; the T at which they crossover is also indicated in Table 1 (in parentheses, in the column displaying ΔE_2)

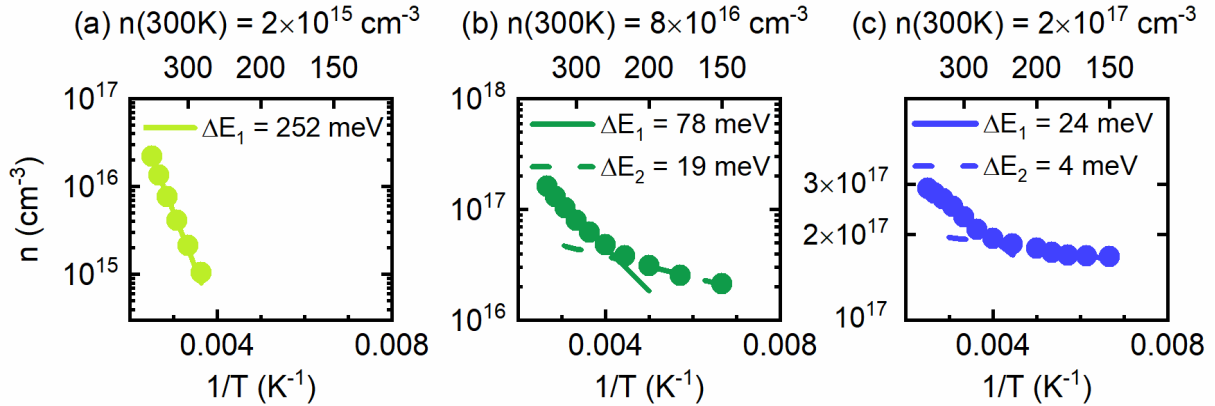


Figure S5. Arrhenius plots of the Hall electron density, n , in (a) lightly- ($n(300\text{ K}) = 2 \times 10^{15} \text{ cm}^{-3}$), (b) moderately- ($n(300\text{ K}) = 8 \times 10^{16} \text{ cm}^{-3}$), and (c) heavily- ($n(300\text{ K}) = 2 \times 10^{17} \text{ cm}^{-3}$) V_S -doped pyrite single crystals. For reference, 300 K, 200 K, and 150 K are indicated on the top of each respective plot. Data are shown as symbols, and fits as lines. Thermal activation energies (ΔE_i) are extracted from the slopes of the fits. Two distinct regions of activation emerge with increasing V_S doping, as discussed above.

The interior Hall mobilities, $\mu(T)$, of lightly-, moderately-, and heavily- V_S -doped crystals are shown in Figures 3b,f,j, of the main text, respectively. In the lightly- V_S -doped crystal, $\mu(T)$ is only weakly T -dependent at high T , indicating that this crystal is likely crossing over from ionized impurity-limited (at lower T) to phonon-limited scattering (at higher T), yielding near-constant μ (Figure 3b). For simplicity, a constant μ of $70 \text{ cm}^2 \text{ V}^{-1} \text{ s}^{-1}$ is thus used to describe $\mu(T)$ (solid line, Figure 3b). In increasingly- V_S -doped crystals (Figures 3f,j), $\mu(T)$ at high T is clearly limited by phonon scattering, with μ increasing upon cooling. A standard approach to analyze phonon-limited

$\mu(T)^{4,6}$ is fitting with a power law ($\mu(T) = CT^{-\alpha}$, where C is a constant and α is a parameter sensitive to the type of scattering phonons), yielding α values of 1.9 and 2.7 in crystals grown at moderate and high $n(300\text{K})$, respectively (solid lines, Figures 3f,j). These α values describe $\mu(T)$ well from 200-400 K and are consistent with values previously reported for pyrite crystals (2.0-2.5).^{4,6,12} Table 1 in the main text lists α for each crystal in this study. Upon cooling below 200 K, power law fits to $\mu(T)$ begin to diverge from the data due to the onset of either bulk ionized impurity scattering or junction (R_J) contributions to R_S , the latter artificially suppressing μ because we are forced to assume $R_I = R_S$ (*i.e.*, no junction influence) when calculating μ . Because we cannot clearly differentiate which effect is dominant, this behavior was not fitted. Again, mitigating the influence of R_J on R_S would offer access to R_I at lower T and enable determination of the true interior $\mu(T)$ across a wider T range. Note that to describe $\mu(T)$ of the specific crystal with $n(300\text{K}) = 3 \times 10^{16} \text{ cm}^{-3}$, an additional term representing ionized impurity scattering was included and thus Matthiessen's rule was employed (*i.e.*, $\mu(T)^{-1} = (CT^{-\alpha})^{-1} + (DT^\beta)^{-1}$, where the product including D (a prefactor) and β (an exponent) represents ionized impurity scattering; $\beta = 2.1$ was used to fit $\mu(T)$ and $R_S(T)$ here). As shown below (Section G), the surface of this crystal was more conductive than others in this study, which suppressed the Hall coefficient (artificially raised n) at $T < 300$ K. This made Arrhenius extraction of ΔE_2 impossible and artificially suppressed $\mu(T)$. Consequently, ΔE_2 and $n_{\infty,2}$ (for $T < 249$ K), and the above $\mu(T)$, were varied to directly fit the R_I contributions to $R_S(T)$ rather than extracting these quantities from separate fits of $n(T)$ and $\mu(T)$. Initial estimates of ΔE_2 , $n_{\infty,2}$, and α values were taken from the crystal with $n(300\text{K}) = 8 \times 10^{16} \text{ cm}^{-3}$. With $n(T)$ and $\mu(T)$ thus described, $R_I(T)$ can be computed in all cases (*e.g.*, the dark blue lines, Figures 3c,g,k).

G. Modeling of surface resistance (R_{Surf}) at low temperature

As touched upon in Section D above, polished⁶ and as-grown⁴ pyrite crystal surfaces have been shown to exhibit Efros-Shklovskii variable-range hopping (ES VRH). In ES VRH,

$$R_{\text{Surf}}(T) = R_0 \exp\left(\frac{T_0}{T}\right)^{1/2}, \quad (\text{S2})$$

where R_{Surf} is the surface sheet resistance, R_0 is the $T \rightarrow \infty$ extrapolation of R_{Surf} , and T_0 is a characteristic temperature.¹⁰ As shown in Figure S3a,b, $\log_{10} R_{\text{Surf}}$ vs. $T^{-1/2}$ of a representative lightly- V_S -doped crystal ($n(300\text{K}) = 2 \times 10^{15} \text{ cm}^{-3}$, lightest green data) is linear below 100 K, consistent with the T -dependence expected from ES VRH, and extraction of R_0 and T_0 yield 1400 Ω and 1900 K, respectively. This is in agreement with previous reports of ES VRH transport on pyrite surfaces.^{4,6} $\log_{10} R_S$ vs. $T^{-1/2}$ of a more heavily V_S -doped crystal ($n(300\text{K}) = 4 \times 10^{16} \text{ cm}^{-3}$, darker green data) is also shown in Figure S3a,b. The surface conduction in this sample is nearly identical to the crystal with $n(300\text{K}) = 2 \times 10^{15} \text{ cm}^{-3}$, with $R_0 = 2200 \Omega$ and $T_0 = 1500$ K. ES VRH can also be confirmed in both samples in an unbiased manner (*i.e.*, without fixing $m = 0.5$, where m is the power in the exponential term of equation S2) using Zabrodskii analysis.⁹ In Figure S3c

are Zabrodski plots of the data in Figures S3a and S3b, where $\ln W$ ($W = -d(\ln R)/d(\ln T)$) is plotted vs. $\ln T$. This linearization of equation S2 yields $\ln W = -m \ln T$, allowing m to be extracted as the negative slope. As shown in Figure S3c, Zabrodski analysis yields $m = 0.46$ and 0.44 for crystals with $n(300\text{K}) = 2 \times 10^{15} \text{ cm}^{-3}$ and $4 \times 10^{16} \text{ cm}^{-3}$, respectively, confirming ES VRH (*i.e.*, $m \approx 1/2$) independent of V_S density.

Based on the above, we model the R_{Surf} of each crystal using equation S2, setting $R_0 = 1200 \Omega$ and $T_0 = 2200 \text{ K}$. These values are extracted from $R_S(T)$ of the crystal with $n(300\text{K}) = 2 \times 10^{15} \text{ cm}^{-3}$ (Figure 2) and agree very reasonably with values extracted for other crystals (see above), and we thus apply them generally to the remainder of the crystals modeled in this study. This is done with one exception: the surface of the crystal with $n(300\text{K}) = 3 \times 10^{16} \text{ cm}^{-3}$ (Figure 2) is atypically conductive, likely because of insufficient polishing (roughened crystal surfaces have been shown to often be more conductive).⁶ This leads to distinctly different R_0 and T_0 of 170Ω and 1700 K , respectively.

H. Modeling of the junction and the junction resistance (R_J)

Generally speaking, the internal junction in this work could be viewed as a p - n homojunction (as described by the Shockley equation), or, if the p -surface is metallic, as a Schottky junction (as described by thermionic emission across a barrier, for example).^{13,14} In fact, for polished pyrite crystal surfaces, which are degenerately doped and yet exhibit ES VRH,⁶ neither model is ideal. Estimates of typical hole densities of pyrite surfaces, however, are large, and surface resistivities are small, on the order of 10^{21} - 10^{22} cm^{-3} and $\sim 10 \text{ m}\Omega \text{ cm}$ (at 100 K), respectively.⁴ Moreover, E_F is typically within 100 meV of the VBM on the surface,^{5,6,8} and we thus treat our pyrite surfaces as metallic-like, with the internal junction having Schottky diode characteristics.

There are four conventional types of transport through a Schottky junction: thermionic emission, diffusion, mixed thermionic emission-diffusion, and tunneling.¹³ In each type, the current density, $J(V, T)$, has an exponential voltage (V) and T dependence of the form,

$$J(V, T) = J_0(e^{qV/k_B T} - 1), \quad (\text{S3})$$

where J_0 is a pre-exponential factor.¹³ The four transport mechanisms only differ in terms of J_0 . In thermionic emission, diffusion, and mixed thermionic emission-diffusion, J_0 is strongly T -dependent and proportional to $e^{-q\phi_B/k_B T}$, where ϕ_B is the Schottky barrier height. In tunnel transport, this prefactor is $e^{-q\phi_B/E_{00}}$, where $E_{00} = \frac{q}{4\pi} \sqrt{\frac{N_D}{\epsilon_S m^*}}$ is nearly T -independent. In the expression for E_{00} , ϵ_S is the relative dielectric constant and m^* is the effective mass of the majority carriers. The thermionic emission, diffusion, and mixed thermionic emission-diffusion theories then differ in terms of the pre-exponential factor in front of the $e^{-q\phi_B/k_B T}$ term.

Since our horizontal transport measurements are conducted under small applied potentials (*i.e.*, in the $V \rightarrow 0$ limit) the junction resistance $R_J(T)$ can be determined from $J(V, T)$ for each transport mechanism using

$$\frac{1}{R_J(T)} = A \left(\frac{\partial J}{\partial V} \right) \Big|_{V \rightarrow 0} \quad (\text{S4})$$

i.e., Ohm's law in the $V \rightarrow 0$ limit, where A is the junction area. Substituting equation S3 into equation S4 and taking the limit gives

$$R_J(T) = \frac{k_B T}{A J_0 q} \quad , \quad (\text{S5})$$

where the T dependence of R_J enters primarily through J_0 . Tunnel transport is thus unable to describe $R_J(T)$, as we observe strongly T -dependent R_J below 200 K (Figures 2 and 3, main text). Trying to determine which of the remaining transport types is manifest, however, is futile because the only difference among the remaining options is in the factors multiplying the $e^{-q\phi_B/k_B T}$ term. R_J is also only accessed in our experiments over a relatively small T range (~ 100 to 175 K). Consequently, we simply model R_J as

$$R_J(T) = R_{0,J} e^{q\phi_B/k_B T} \quad , \quad (\text{S6})$$

where $R_{0,J}$ is the $T \rightarrow \infty$ extrapolation of R_J . For simplicity, we assume $R_{0,J}$ is T -independent. We acknowledge that this is not necessarily the case, however. For example, in thermionic emission $R_{0,J}$ has an inverse T -dependence,¹³ but we simply assume that this is weak and inconsequential relative to the $e^{q\phi_B/k_B T}$ term. We thus focus our efforts on determining and interpreting the *barrier heights* (ϕ_B) rather than $R_{0,J}$.

In combination with $R_{\text{Surf}}(T)$ (described by ES VRH, see Section G above) and $R_I(T)$ (described by diffusive transport, see Section F above), $R_S(T)$ can now be modeled using the circuit network in Figure 1b using only two free parameters ($R_{0,J}$ and ϕ_B), describing the R_J contributions to $R_S(T)$. The resultant $R_J(T)$ of lightly-, moderately-, and heavily- V_S -doped crystals are shown with light blue lines in Figures 3c,g,k, respectively, in the main text. $R_{0,J}$ and ϕ_B extracted from these $R_S(T)$ are tabulated in Table 1 of the main text. The heavily- V_S -doped crystal (Figures 3i-l) yields $R_{0,J}$ and ϕ_B values of $5 \times 10^{-9} \Omega$ and 270 meV, respectively. For thermionic emission-dictated transport, $R_{0,J} = \frac{k_B}{A A^* q T}$, where A^* is Richardson's constant.¹³ For pyrite, using an electron effective mass of $0.45 m_e$,¹⁵ where m_e is the electron mass, $A^* = 6 \times 10^5 \text{ A m}^{-2} \text{ K}^{-2}$, and $R_{0,J}$ can be estimated as $5 \times 10^{-8} \Omega$, within an order of magnitude of the fit result. $R_{0,J}$, however, varies strongly from crystal to crystal, ranging from 10^{-4} - $10^{-15} \Omega$ (Table 1). Since differences in $R_{0,J}$ are the only way to resolve the remaining transport types, this crystal-to-crystal variability precludes any conclusion as to which mechanism dictates transport through this internal junction. Finally, note that at low $n(300\text{K})$ (Figure 3c), $R_J(T)$ is shown as a dotted light blue line, as R_J is not required to achieve a quantitative description of $R_S(T)$ because carrier freeze-out directly gives way to surface conduction upon cooling. This $R_J(T)$ curve instead establishes an upper bound on the ϕ_B (500 meV) necessary for any R_J influence to emerge, assuming a thermionic-emission-estimated $R_{0,J} = 5 \times 10^{-8} \Omega$. The ability to model $R_S(T)$ without inclusion of the junction is thus unsurprising, as only two heavily- V_S -doped crystals exhibit a ϕ_B this large.

I. Band bending calculations of heavily doped pyrite crystals and Au/Si Schottky diodes

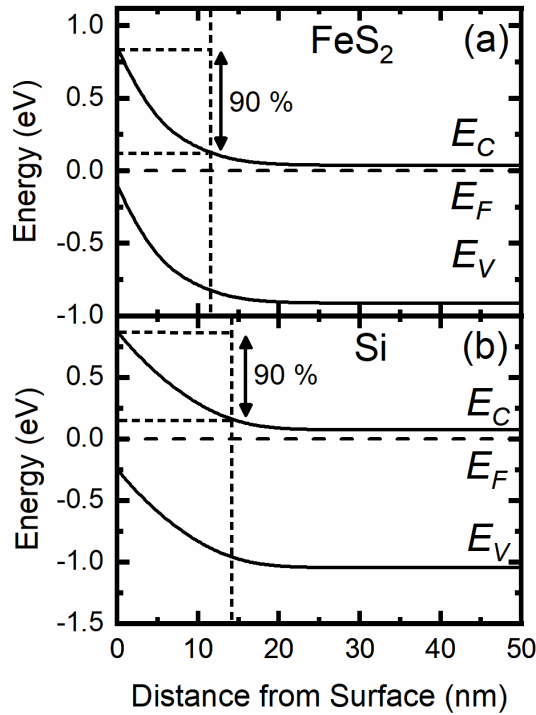


Figure S6. Calculated equilibrium band bending at 300 K for (a) heavily Co-doped pyrite and (b) heavily- n -doped Si contacted with Au (which forms a Schottky contact with a barrier height, $\phi_B \sim 0.8$ eV).¹⁶ In (a), the Fermi level (E_F) is pinned ~ 100 meV above the valence band maximum (E_V) at the surface. Again, the interior of the crystal is assumed to be compensated with an acceptor concentration (N_A) of 7.5×10^{17} cm⁻³. Calculations include two donors, V_S and Co, with activation energies (ΔE) and donor densities of 225 meV and 16 meV, respectively. The V_S and Co donor densities used in the calculations are 9×10^{18} cm⁻³ and 5×10^{18} cm⁻³, respectively. The latter is chosen to yield an electron density (n) far into the crystal interior consistent with experiment ($\sim 2 \times 10^{18}$). In (b), sufficient surface Fermi level pinning is induced to yield $\phi_B = 0.8$ eV, using a band gap of 1.12 eV. To describe interior n -doping, a hydrogenic ($\Delta E \approx 30$ meV) donor with density 2.6×10^{18} cm⁻³ is used. In each case, >90 % of band bending occurs in the top ~ 12 -14 nm.

Supporting Information References

- (1) Snider, G. 1D Poisson <https://www3.nd.edu/~gsnider/>.
- (2) Voigt, B.; Moore, W.; Manno, M.; Walter, J.; Jeremiason, J. D.; Aydil, E. S.; Leighton, C. Transport Evidence for Sulfur Vacancies as the Origin of Unintentional *n*-Type Doping in Pyrite FeS₂. *ACS Appl. Mater. Interfaces* **2019**, *11*, 15552–15563.
- (3) Ashcroft, N. W.; Mermin, N. D. *Solid State Physics*; Harcourt College, 1976.
- (4) Walter, J.; Zhang, X.; Voigt, B.; Hool, R.; Manno, M.; Mork, F.; Aydil, E. S.; Leighton, C. Surface Conduction in *n*-Type Pyrite FeS₂ Single Crystals. *Phys. Rev. Mater.* **2017**, *1*, 065403.
- (5) Cabán-Acevedo, M.; Kaiser, N. S.; English, C. R.; Liang, D.; Thompson, B. J.; Chen, H.; Czech, K. J.; Wright, J. C.; Hamers, R. J.; Jin, S. Ionization of High-Density Deep Donor Defect States Explains the Low Photovoltage of Iron Pyrite Single Crystals. *J. Am. Chem. Soc.* **2014**, *136*, 17163–17179.
- (6) Limpinsel, M.; Farhi, N.; Berry, N.; Lindemuth, J.; Perkins, C. L.; Lin, Q.; Law, M. An Inversion Layer at the Surface of *n*-Type Iron Pyrite. *Energy Environ. Sci.* **2014**, *7*, 1974–1989.
- (7) Bronold, M.; Tomm, Y.; Jaegermann, W. Surface States on Cubic *d*-Band Semiconductor Pyrite (FeS₂). *Surf. Sci.* **1994**, *314*, L931–L936.
- (8) Ennaoui, A.; Fiechter, S.; Pettenkofer, C.; Alonso-Vante, N.; Bükler, K.; Bronold, M.; Höpfner, C.; Tributsch, H. Iron Disulfide for Solar Energy Conversion. *Sol. Energy Mater. Sol. Cells* **1993**, *29*, 289–370.
- (9) Zabrodskii, A. G. The Coulomb Gap: The View of an Experimenter. *Philos. Mag. B* **2001**, *81*, 1131–1151.
- (10) Shklovskii, B. I.; Efros, A. L. *Electronic Properties of Doped Semiconductors*; Springer: Berlin, 1984.
- (11) Ray, D.; Voigt, B.; Manno, M.; Aydil, E. S.; Leighton, C.; Gagliardi, L. Sulfur Vacancy Clustering and Its Impact on Electronic Properties in Pyrite FeS₂. *Chem. Mater.* **2020**, *32*, 4820–4831.
- (12) Tomm, Y.; Schieck, R.; Ellmer, K.; Fiechter, S. Growth Mechanism and Electronic Properties of Doped Pyrite (FeS₂) Crystals. *J. Cryst. Growth* **1995**, *146*, 271–276.
- (13) Sze, S. M. *Physics of Semiconductor Devices*; John Wiley & Sons: New York, 1981.
- (14) Bube, R. H. *Photoelectronic Properties of Semiconductors*; Cambridge University Press: Cambridge, 1992.
- (15) Karguppikar, A. M.; Vedeshwar, A. G. Transport Properties of Thin Iron Pyrite Films. *Phys. Status Solidi* **1986**, *95*, 717–720.
- (16) Chang, C. Y.; Sze, S. M. Carrier Transport Across Metal-Semiconductor Barriers. *Solid State Electron.* **1970**, *13*, 727–740.